

Neutrino type identification for atmospheric neutrinos in a large homogeneous liquid scintillation detector

Jiayi Liu,^{1,2,*} Fanrui Zeng,^{3,*} Hongyue Duyang,^{3,†} Wanlei Guo,¹ Xinhai He,¹ Teng Li,^{3,‡} Zhen Liu,^{1,§} Wuming Luo,^{1,¶} Wing Yan Ma,^{3,**} Xiaohan Tan,³ Liangjian Wen,¹ Zekun Yang,³ and Yongpeng Zhang^{1,††}

¹*Institute of High Energy Physics, Chinese Academy of Sciences, Beijing 100049, China*

²*School of Physical Sciences, University of Chinese Academy of Science, Beijing 100049, China*

³*Shandong University, Jinan, China, and Key Laboratory of Particle Physics and Particle Irradiation of Ministry of Education, Shandong University, Qingdao 266237, China*

Atmospheric neutrino oscillations are important to the study of neutrino properties, including the neutrino mass ordering problem. A good capability to identify neutrinos' flavor and neutrinos against antineutrinos is crucial in such measurements. In this paper, we present a machine-learning-based approach for identifying atmospheric neutrino events in a large homogeneous liquid scintillator detector. This method extracts features that reflect event topologies from PMT waveforms and uses them as input to machine learning models. In addition, neutron-capture information is utilized to achieve neutrino versus antineutrino discrimination. Preliminary performances based on Monte Carlo simulations are presented, which demonstrate such detector's potential in the future measurements of atmospheric neutrinos.

I. INTRODUCTION

Atmospheric neutrinos constitute an important natural neutrino source for investigating fundamental neutrino properties. Produced by cosmic rays interacting with the Earth's atmosphere, atmospheric neutrinos span wide energy spectra and oscillation baseline lengths, making them well-suited for studying neutrino oscillations. The most notable example is the discovery of neutrino oscillations by the Super-Kamiokande experiment in 1998 [1]. One of the biggest questions in neutrino physics that future atmospheric neutrino measurements could solve is the sign of Δm_{31}^2 and Δm_{32}^2 , commonly known as the neutrino mass ordering (NMO) (or neutrino mass hierarchy) problem. Matter effects, due to charge-current interactions between neutrinos and electrons in matter when atmospheric neutrinos pass through the earth, could help experiments to solve the problem by amplifying the differences between NO and IO [2, 3]. Such measurements, however, are also affected by uncertainties such as the unknown value of the CP-violating phase (δ_{CP}) and the θ_{23} octant ambiguity. The next-generation experiments, such as Hyper-Kamiokande [4, 5], KM3Net/ORCA [6, 7] and IceCube-Upgrade [8], designed to measure atmospheric neutrino oscillations and solve the NMO problem with gigantic water Cherenkov detectors, are currently under construction.

A different experimental configuration that can solve the NMO problem is the medium baseline (~ 50 km) re-

actor antineutrino oscillation in vacuum or near-vacuum conditions. This configuration has the advantage that it does not depend on δ_{CP} and the θ_{23} octant. The only experiment on the horizon with this configuration is the Jiangmen Underground Neutrino Observatory (JUNO), currently under construction in China. It is designed to determine NMO with a 20kton homogeneous liquid scintillator (LS) detector by measuring reactor electron antineutrino ($\bar{\nu}_e$) oscillations [9, 10]. It is also worth noting that the two configurations are complementary, and the synergy between them can greatly enhance the total sensitivity in a global fit [11–13]. Therefore, if atmospheric (anti)neutrino oscillations can also be measured in a large homogeneous LS detector like JUNO itself, its NMO sensitivity can be maximized by a joint analysis with both reactor and atmospheric neutrino oscillations in the same detector.

Atmospheric neutrino oscillation measurements in an LS detector, however, are very challenging. While such detectors has been utilized by experiments such as KamLAND [14], Borexino [15, 16], Daya Bay [17, 18], RENO [19, 20], and Double Chooz [21, 22] for reactor and solar neutrino measurements, they have never been used for atmospheric neutrinos. This is mostly due to two difficulties. First, LS detectors are traditionally believed to lack directional measurement capability, which is mandatory for atmospheric neutrino oscillation measurements to determine the neutrino oscillation baseline length. Second, because the atmospheric neutrino flux is a mixture of muon (anti)neutrino ($\nu_\mu/\bar{\nu}_\mu$) and electron (anti)neutrinos ($\nu_e/\bar{\nu}_e$), the neutrino flavor needs to be identified in the detector to determine the oscillation probabilities. Moreover, the ability to identify neutrinos against antineutrinos is important since matter effects distort their oscillation probability in opposite ways. While experiments lacking such capability still get some sensitivity to NMO from small differences in fluxes and cross sections for neutrinos and antineutrinos, the dis-

* Jiayi Liu and Fanrui Zeng contributed equally to this work.

† Corresponding author: duyang@sdu.edu.cn

‡ Corresponding author: tengli@sdu.edu.cn

§ Corresponding author: liuzhen@ihep.ac.cn

¶ Corresponding author: luowm@ihep.ac.cn

** Corresponding author: wingyanma@sdu.edu.cn

†† Corresponding author: ypzhang1991@ihep.ac.cn

criminating power between the neutrinos and antineutrinos certainly helps to disentangle NMO and CP violation phase and increase the sensitivity. However, such flavor identification and neutrino/antineutrino discrimination have never been achieved in LS detectors before.

Neutrino flavors are reflected in the flavors of outgoing charged leptons in neutrino-nucleus charged current (CC) interactions. Therefore, a detector's capability of neutrino flavor identification largely relies on the identification of charged leptons, *i.e.*, e^\mp in $\nu_e/\bar{\nu}_e$ -CC, and μ^\mp in $\nu_\mu/\bar{\nu}_\mu$ -CC interactions. In a water Cherenkov detector, this task is achieved by identifying the sharpness of the Cherenkov ring. But this approach is not feasible in an LS detector, where Cherenkov light is typically about two orders of magnitude weaker than scintillation light. Neutrino versus antineutrino identification is even more challenging. The most prominent difference between neutrino and antineutrino interactions is the charge of outgoing leptons in CC interactions. However, it is impractical to magnetize a modern neutrino detector with a kilotons-scale mass to identify the particle charge. Other handles may help in this task including the differences in event kinematics and neutron multiplicity in the (anti)neutrino interactions. One recent example in a water Cherenkov detector is the atmospheric neutrino oscillation measurement by Super-Kamiokande with neutron-tagging [23]. Super-Kamiokande with gadolinium loading is expected to improve further the neutrino/antineutrino discrimination with better neutron-tagging efficiency [24, 25]. Besides, event inelasticity is also proposed to be used in IceCube-upgrade and KM3NET/ORCA to separate neutrinos/antineutrinos and improve the oscillation sensitivity to NMO [26, 27]. LS detectors, on the other hand, are known to have excellent neutron-tagging efficiency, but event kinematics such as inelasticity measurements are very difficult with traditional reconstruction methods.

Recently, we reported a novel method of directionality measurement in an LS detector that solves the first difficulty in utilizing an LS detector for atmospheric neutrino oscillation measurements [28]. This method extracts features relevant to the event topology in the detector from PMT waveforms and uses them as input to machine learning (ML) models trained to find the event directionality. In this paper, we further explore the possibility of flavor identification in an LS detector such as JUNO for atmospheric neutrinos with a methodology based on a similar ML principle. A statistical neutrinos versus antineutrinos identification is also demonstrated with additional help from neutron capture information.

This paper is organized as follows. Section II describes the detector and simulation used in the work. Section III A presents the methodology of 3-label identification, *i.e.*, $\nu_\mu/\bar{\nu}_\mu$ -CC versus $\nu_e/\bar{\nu}_e$ -CC versus neutral current (NC) identification, and section III B presents neutrino vs anti-neutrino identification. The identification performance is presented in section IV, and more details are further discussed in section V. Finally section VI summarizes the study.

II. DETECTOR AND SIMULATION

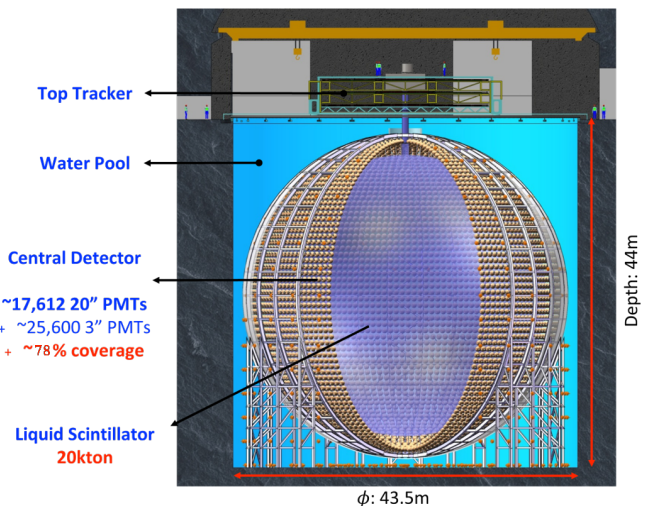


Figure 1. Drawing of the JUNO detector design.

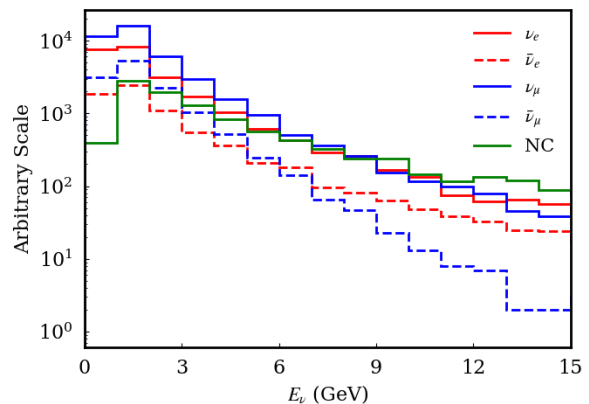


Figure 2. The neutrino energy distribution of the Honda-flux sample used for performance evaluation in this work. The sample is divided into five classes: $\nu_\mu/\bar{\nu}_\mu/\nu_e/\bar{\nu}_e$ -CC and NC, represented by different colors.

The JUNO central detector (CD) design and simulation [29, 30] are used to demonstrate the method. A schematic view of the detector is shown in Fig. 1. It contains 20kton LS in an acrylic sphere with a radius of 17.7 m. 17,612 20-inch PMTs [31] are installed facing inward to collect light produced by charged particles with a total PMT coverage of 75%. In addition, 25,600 3-inch PMTs [32] provide additional 3% coverage. For simplicity, only 20-inch PMTs are used in this work. The LS consists of linear alkylbenzene as the detection medium, 2.5 g/L 2,5-diphenyloxazole (PPO) as the fluor and 3 mg/L p-bis-(o-methylstyryl)-benzene (bis-MSB) as the wavelength shifter [33]. More details about the JUNO detector can be found in Ref. [9].

Neutrino interactions in the detector are simulated mainly by the GENIE event generator (v3.0.6) [34, 35], and the NuWro event generator [36] is used as an independent check. The detector response is simulated based on Geant4 [37, 38]. Various electronic effects, including PMT dark noise, time transition spread (TTS), *etc.*, are also implemented. The detailed PMT simulation parameters are the same as in Ref. [28].

Three independent neutrino interaction samples are produced to train and validate the machine learning models, each including five categories of events: ν_μ -CC, $\bar{\nu}_\mu$ -CC, ν_e -CC, $\bar{\nu}_e$ -CC and NC. The first sample is simulated with GENIE and has roughly flat visible energy distributions and similar statistics (about 70 k) for each category to avoid introducing any energy dependence in the model training (referred to as the flat sample). The second is simulated with GENIE and a more realistic flux taken from the calculation of Honda *et al.* [39] for the JUNO site without the overburden mountain. This sample is used for performance evaluation with total statistics of about 95 k. The neutrino energy spectrum of the Honda-flux sample is shown in Fig. 2. The last one is simulated with NuWro with similar statistics to the Honda-flux sample to test the robustness of the performance with a different generator (referred to as the NuWro sample). For each sample, events with visible energy between 0.5 and 15 GeV are selected for this study.

III. METHODOLOGY

Neutrino-nucleus interactions in an LS detector are complicated in the few-GeV energy region which is the most sensitive energy region to NMO. In a typical $\nu_\mu/\bar{\nu}_\mu$ -CC event, the μ^\mp from the primary interaction deposits its energy quickly and leaves a long track in LS. Various hadrons such as n , p , π^0 and π^\pm can also be produced through primary and secondary interactions. Most charged hadrons and π^0 s produce showers while rapidly depositing their energies in LS, with the exception that π^\pm s behaves similarly to μ^\pm s. For a $\nu_e/\bar{\nu}_e$ -CC event, the event topology in the LS is similar to that of $\nu_\mu/\bar{\nu}_\mu$ -CC except that e^\mp from the primary interaction also produces a shower. The primary charged lepton and hadrons together trigger the detector promptly (the prompt trigger). For an NC event, the hadron part is similar to a CC event, yet the outgoing neutrino is invisible.

Tracks and showers propagate through LS and produce scintillation light. Scintillation light seen by a PMT is the superposition of light from many points along the track or shower. The time evolution of scintillation light seen by PMTs is therefore determined by the event topology in the detector. Fig. 3 shows the PE time distributions ($n_{PE}(t)$) of PMTs at different angles with respect to an electron and a muon simulated at the detector center with the same kinetic energy (1 GeV) and direction. It is observed that the two particles exhibit distinct $n_{PE}(t)$ shapes. This is mostly because electron showers are gen-

erally much shorter than muon tracks at the same energy in the LS. The differences in the $n_{PE}(t)$ distribution are then reflected in the PMT waveforms. Therefore, it is possible to use the information from PMT waveforms of the prompt trigger to identify different event topologies and distinguish the three flavors of atmospheric neutrino events.

While it is impossible to discriminate neutrino and antineutrino interactions event by event without identifying the charge of the outgoing lepton, the task can be done statistically with help from several handles. The first one is their differences in event kinematics. In CC interactions, neutrinos tend to transfer more energy to hadrons than anti-neutrinos with the same energy due to the V-A structure of $\nu/\bar{\nu}$ interactions. This leads to a larger visible hadronic energy fraction ($y_{vis} = E_{had,vis}/E_{vis}$, where $E_{had,vis}$ is the visible energy caused by hadrons and E_{vis} is the total visible energy of the event) for neutrino interactions (Fig. 4). As mentioned in Ref. [28], one advantage of LS detectors over water Cherenkov detectors is that the hadrons produced from atmospheric neutrinos are also mostly visible. To help illustrate this point, Fig. 5 shows an example of a simulated neutrino interaction with clear separation between the leptonic and hadronic energies. Since both the charged leptons and most hadrons in the final state of CC events deposit their energy within the prompt trigger, the y_{vis} information is also reflected in the event topology and finally also in the trigger's PMT waveforms.

The second handle is the neutron information. Neutrons can be produced both in the primary neutrino-nucleus interactions and also in secondary interactions. Antineutrino interactions generally tend to produce more primary neutrons due to charge conservation. The number and spacial distribution of secondary neutrons are also related to the types and kinematics of the primary particles. Neutron multiplicities (including both primary and secondary neutrons) for different neutrino CC interactions are shown in Fig. 4. The neutrons produced dissipate their kinetic energy and are eventually captured mostly by hydrogen nuclei with a time constant of about 200 μ s. The average distance from the primary neutron capture position to the neutrino interaction vertex is about 0.5 m in LS according to simulation, and the capture positions for secondary neutrons are much more dispersed. 2.2 MeV γ s are then released and create delayed triggers. Another advantage of LS detectors such as JUNO is the excellent efficiency in tagging such neutron captures compared to Water Cherenkov detectors. The information from delayed triggers caused by neutron captures therefore also helps to distinguish neutrinos from antineutrinos. More details on how to utilize the delayed trigger information will be discussed in Sec. III B.

Based on the discussion above, the identification task of atmospheric neutrino interactions is broken down into two steps: firstly to identify the μ -like ($\nu_\mu/\bar{\nu}_\mu$ -CC), e -like ($\nu_e/\bar{\nu}_e$ -CC), and NC-like events against each other (referred to as the 3-label identification), and secondly

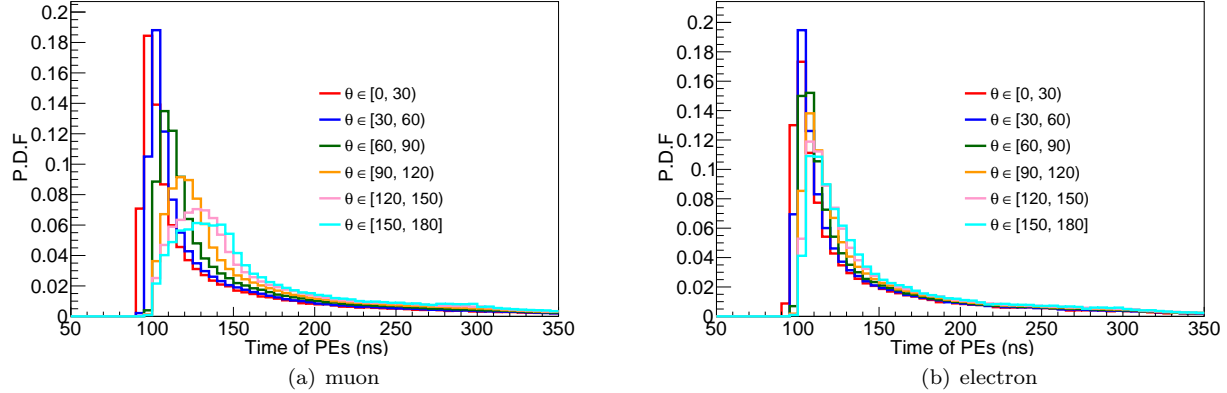


Figure 3. The normalized time distributions of PEs for PMTs at different angles (θ , in degree) to (a) a muon and (b) an electron with the same kinetic energy (1 GeV), vertex position (at the center of the detector) and initial direction (along the positive x-axis). The PMT angle θ is the intermediate angle between the particle direction and the line connecting the middle point of the particle track and the PMT. Distinct shapes can be observed for the two types of particles.

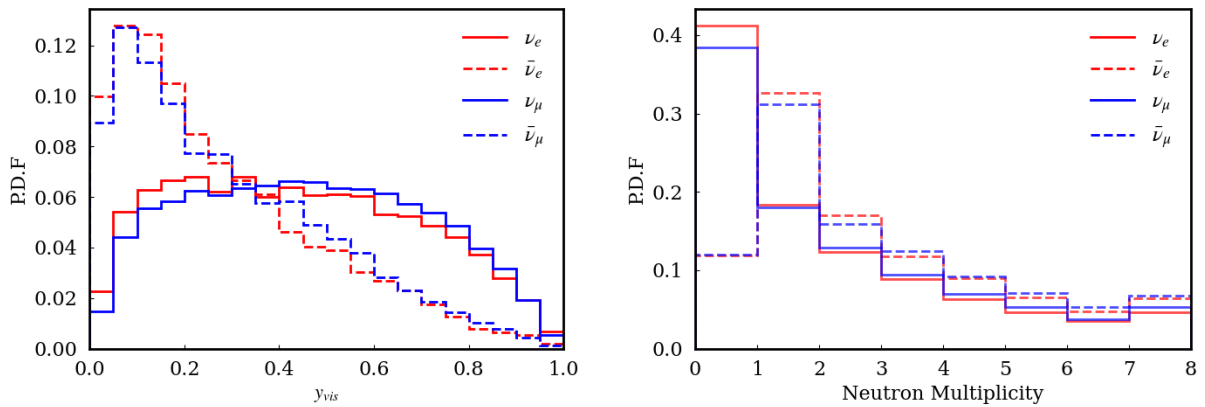


Figure 4. y_{vis} (left) and neutron multiplicity (right) distributions for $\nu_\mu/\bar{\nu}_\mu/\nu_e/\bar{\nu}_e$ -CC interactions in the Honda-flux sample. Full detector simulation is included. The distributions are normalized for a shape-only comparison.

to discriminate ν -like from $\bar{\nu}$ -like events (referred to as the 2-label identification). The details of each step are described in the following subsections. Sec. V also briefly discusses other possible strategies.

A. 3-label flavor identification

In this step, atmospheric neutrino events are classified as μ -like, e -like, or NC-like using information from the 20-inch PMTs' waveforms in the prompt triggers. A machine-learning-based method similar to that in Ref. [28] is used. This method extracts features from PMT waveforms in 1 ns bins as inputs to ML models. These features include the hit time of the earliest photon (first hit time, FHT), the total charge, the slope of the waveform in the first 4 ns after FHT, the charge ratio in the first 4 ns after FHT to the total, the time and amplitude of the waveform's maximum bin, and other fea-

tures such as median time and four moments (mean, std, skewness, kurtosis) of the waveform in a 1000 ns trigger window which describes the reconstructed waveforms in a more subtle way. A deconvolution and noise-reduction algorithm [40, 41] is applied to the waveform before the feature extraction to improve the feature quality. More details of the feature extraction are described in Ref. [28].

The PMT features from all 20-inch PMTs of the JUNO CD form spherical image-like data. Two different ML models from Ref. [28] are used to deal with this kind of data: the Deepsphere [42] model which processes spherical data directly and the PointNet++ [43] model which inputs data as a 3D point cloud. The model architectures remain mostly the same except that the activation functions of the last layer are changed to softmax to output three scores representing the probability of the event being μ -like, e -like, or NC-like respectively. The sum of these three scores is one and an event is classified to the category with the largest score by default.

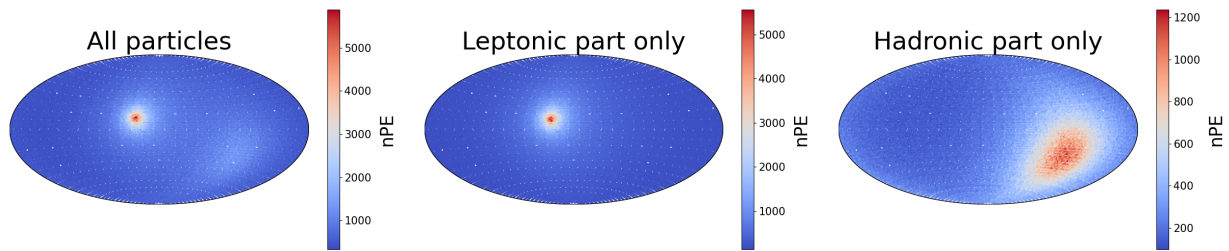


Figure 5. Event display pictures of a simulated ν_e -CC interaction showing the PMT charges (nPE) from all particles (left), leptonic part only (middle), and hadronic part only (right). The PMT charge values are represented by colors and are projected onto a planer surface following the Mollweide projection method.

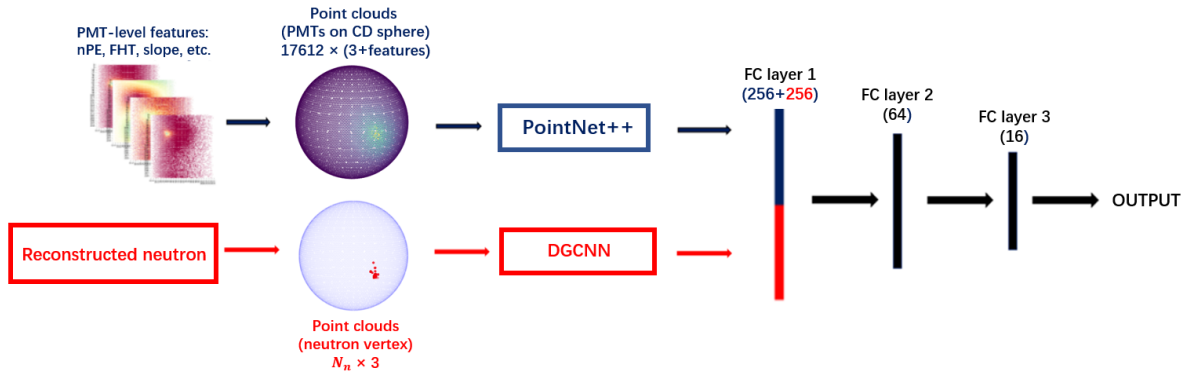


Figure 6. Schematic diagram of the model architecture used by $\nu/\bar{\nu}$ identification strategy 1. The model consumes two types of inputs: PMT features from the prompt trigger processed by PointNet++, and neutron-capture vertex cloud processed by DGCNN. The outputs of PointNet++ and DGCNN are input to fully connected (FC) layers to predict the final scores representing the probability of the event being caused by neutrinos or antineutrinos.

B. 2-label $\nu/\bar{\nu}$ identification

The identification of $\nu/\bar{\nu}$ interactions relies on their differences in event kinematics, neutron multiplicity, and the spatial distribution of neutron-capture vertices. The event kinematics information contained in the PMT waveforms of the prompt trigger is also reflected in the waveform features described in the previous subsection, including the y_{vis} information discussed in section III. The neutron information, on the other hand, is reflected in the delayed triggers which are selected with energy between 2 and 2.7 MeV, and the delay time between 10 μ s and 1 ms. Therefore, the information from the prompt and delayed triggers needs to be combined for the task. Two different strategies are developed and described here.

1. Strategy 1

In this strategy, neutron-capture vertices are first reconstructed using the method from Ref. [44]. The reconstructed vertices from multiple selected delayed triggers form a new 3D point cloud that is input to the ML model together with the one formed by PMT waveform

features from the prompt trigger. In this way, most of the neutron-capture information, including their spatial distribution, is conserved. The overall structure of the ML model for strategy 1 is illustrated in Fig. 6. Similar to the 3-label identification in step 1, the PMT waveform features from the prompt trigger are fed into a model based on PointNet++. For the neutron-capture vertices, given that the number of neutrons is usually less than 100 for an atmospheric neutrino event, the size of the point-cloud data is fixed to 128 points, with zero-padding if the number of selected neutron-capture candidates is less than 128. This point-cloud data of neutrons is fed into an individual Dynamic Graph CNN (DGCNN)-based model [45]. Compared to traditional GCNN models, DGCNN is able to recover the neighborhood topology of point clouds with edge information, making it more suitable for describing spatial relationships of sparse point clouds. The DGCNN-based model output is then concatenated with the PointNet++-based model output with a set of fully-connected layers.

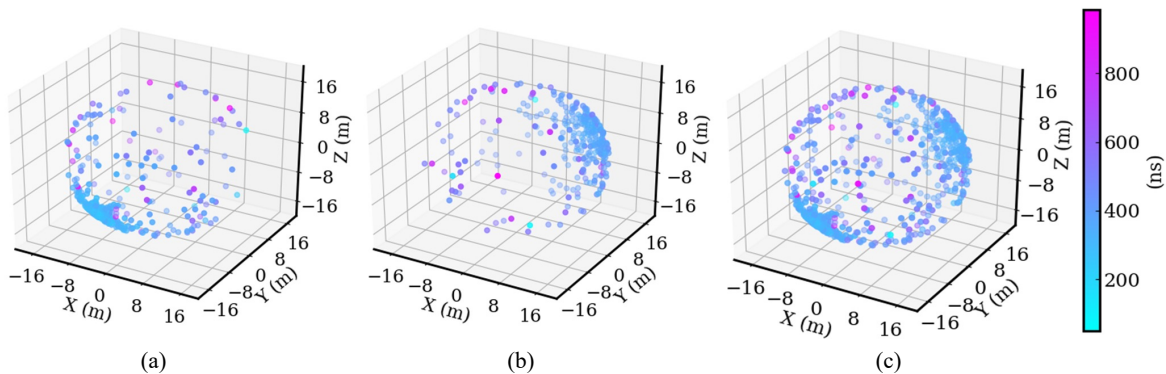


Figure 7. Illustration of the trigger-merging technique used by strategy 2. (a) and (b) show two delayed triggers selected as neutron-capture candidate triggers, and (c) shows the new merged one. Fired PMTs are shown as dots on the figures, with color representing FHT values of the hits.

2. Strategy 2

Instead of reconstructing individual neutron-capture vertices, this strategy merges multiple delayed triggers into one by summing up the charges from multiple selected delayed triggers for each PMT, and taking the FHT value as the earliest among them (Fig. 7). The two features (FHT and charge) are then used as extra features to the ML model together with features from the prompt trigger. This strategy does not rely on neutron-capture reconstruction algorithms and provides a fast and coherent way of utilizing features from both the prompt trigger and the delayed trigger. A DeepSphere-based model with the same architecture as used in the 3-label identification is used for the demonstration of this strategy. For both strategies, the final output is a 2-label classifier, with 2 scores representing the probability of an event being ν -like or $\bar{\nu}$ -like respectively. The models are then trained separately for the ν_μ vs $\bar{\nu}_\mu$ and ν_e vs $\bar{\nu}_e$ identification.

IV. PERFORMANCE

The 3-label and 2-label ML models are trained with the flat sample labeled by event categories. The trained models are then applied to the Honda flux sample for performance evaluation in a more realistic situation. The efficiency, purity, and accuracy of event selection depend on the cuts on those scores, which should be optimized by future analyses. To evaluate the model performances independent from the choices of selection cuts, the receiver operating characteristic (ROC) curve and the area under the ROC curve (AUC) are used [46]. They have the advantage of independence from the score cut choice, and do not suffer from a class imbalance in the dataset if there is one. While the typical ROC curve and AUC are designed for binary classifications, the concepts are extended to an N -class classification in this work. For a given class i , the ROC curve and corresponding AUC

score are obtained by converting the N -class classification to a “class i vs others” binary classification. The efficiency of class i is defined as the fraction of events in class i with the score associated with the class greater than a certain cut value. In contrast, the selection efficiency of “others” is calculated as the fraction of events with the score lower than the cut value. By varying the cut value from 0 to 1, one can calculate the corresponding two efficiencies above and subsequently draw the ROC curve of “class i vs others”, from which an AUC value is obtained. Finally, the total AUC score is defined as the arithmetic mean of all “class i vs others” binary classification scores. The performance of the 3-label and 2-label models are presented in the following subsections separately.

A. 3-label flavor identification

Fig. 8 shows the distributions of the μ -like score and e -like score output by the two 3-label ML models. (The NC-like scores are not shown since NC is a background.) Clear separations are observed for the three event classes. Three ROC curves can be obtained from the score distributions, using the “class i vs others” method. Fig. 9 shows the ROC curves and AUC values for the two ML models using events across all energies. Such ROC curves are also calculated for events in different visible energy bins and the corresponding total AUC values are obtained by averaging over the AUC value of each class. Fig. 10 compares the total AUC values as a function of visible energy for the two ML models. The AUC values are rather consistent, indicating that the performances of the two models are very close.

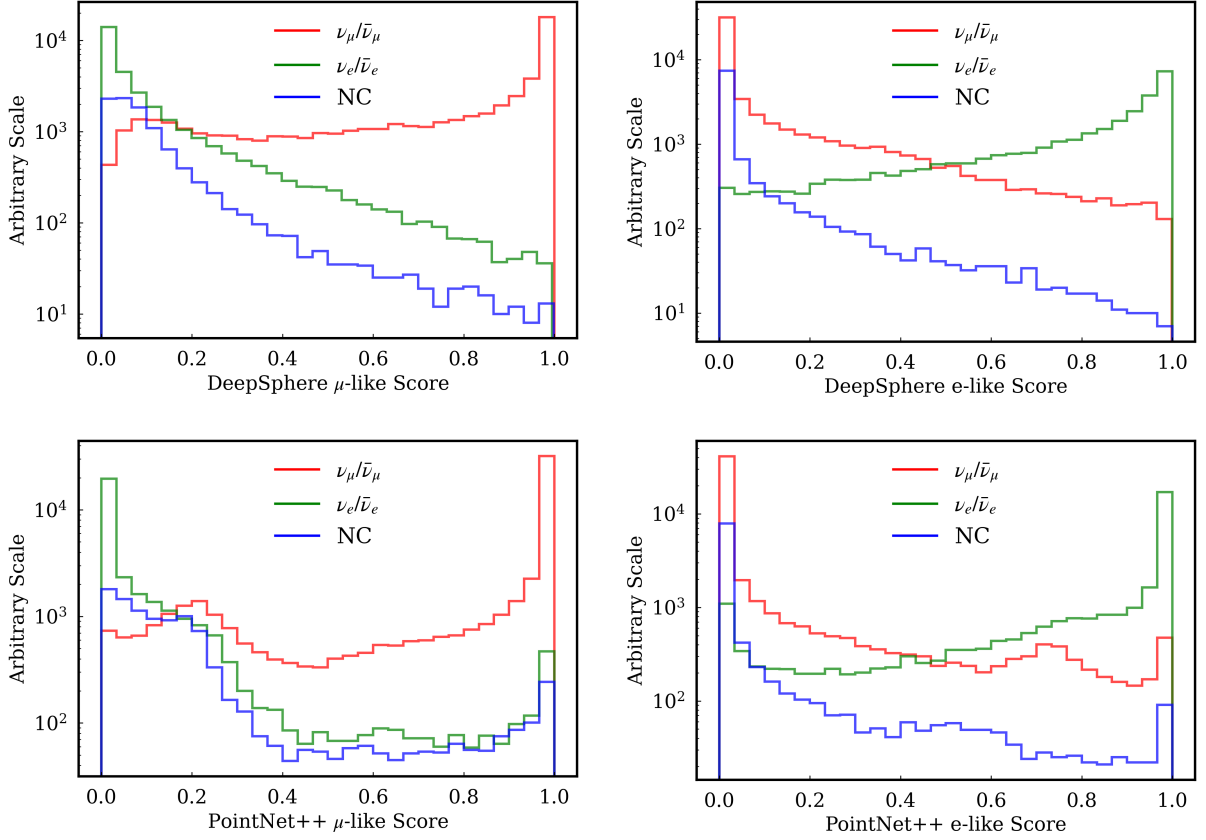


Figure 8. Distributions of the μ -like score (left) and e -like score (right) by the Deepsphere (top) and PointNet++ (bottom) models. True $\nu_\mu/\bar{\nu}_\mu$ -CC, $\nu_e/\bar{\nu}_e$ -CC and NC events are shown in different colors.

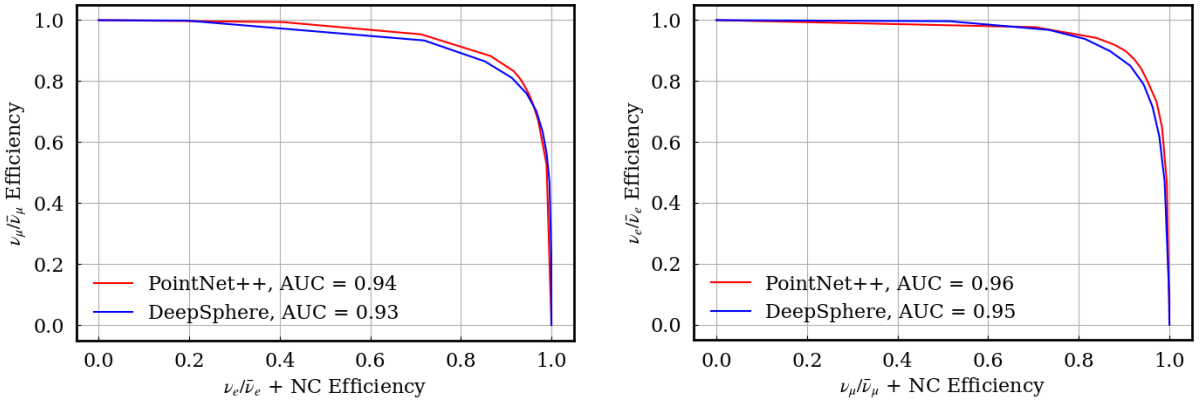


Figure 9. ROC curves of the 3-label identification by the two ML models using events across all energies. For each ROC plot, the vertical axis shows the selection efficiency of one of the three classes, and the horizontal axis shows the efficiency of the other two combined. The corresponding AUC values are also listed.

B. 2-label $\nu/\bar{\nu}$ identification

Similar to the 3-label identification, the performances of the $\nu/\bar{\nu}$ identification are evaluated in terms of ROC curve and AUC values using the Honda-flux sample.

The ML model output score distributions are shown in Fig. 11, where distinct shapes are obtained for neutrinos and antineutrinos. The selection efficiencies of (anti)neutrinos for the ROC curve are obtained by selecting events with scores above (below) various cut values.

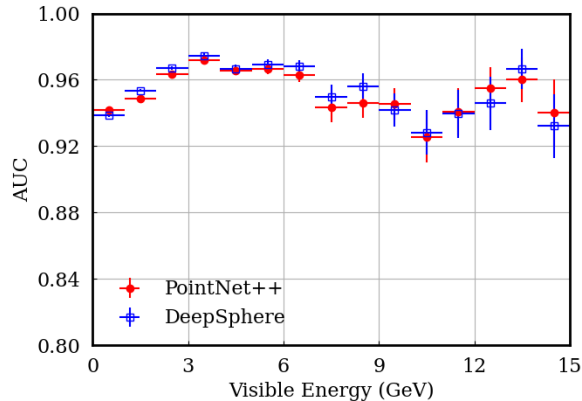


Figure 10. The total AUC values of the 3-label identification as functions of visible energy for the two models. Error bars show the statistical uncertainties in each energy bin obtained with the bootstrap method [47].

The ROC and AUC comparison of the two strategies are shown in Fig. 12 and 13. The two strategies give similar $\nu/\bar{\nu}$ identification performances. The remaining differences could be caused by the differences in the models and how the information of the captured neutron candidates is handled. In addition, the performance for $\nu_\mu/\bar{\nu}_\mu$ identification is better than that of $\nu_e/\bar{\nu}_e$. This could be mainly attributed to more (less) distinctive detector response of muons (electrons) with respect to hadrons in LS.

V. DISCUSSION

A. Dependence on event generators

In this work, event identification utilizes the event topology information reflected by the PMT features in the prompt trigger and the neutron-capture information from the delayed triggers. Both pieces of information rely on the simulation of the neutrino-nucleus interaction process, which could be different for various event generators. To check the dependence of the PID performance on the neutrino-nucleus interaction simulation, an independent sample was produced using the NuWro event generator, as mentioned in II. The models trained with the flat sample produced by GENIE are applied to this NuWro sample. Fig. 14 compares the PID performance obtained from the GENIE and NuWro Honda-flux testing samples, using the PointNet++ model and strategy 1 of neutron-capture information handling as an example. Despite some small discrepancies, the performance is mostly consistent between the two samples. This additional check suggests that the ML models in this work do not suffer from apparent dependence on the event generator.

B. Score cut optimization

After the flavor and $\nu/\bar{\nu}$ identification, the candidate atmospheric neutrino events shall be categorized into ν_μ -CC, $\bar{\nu}_\mu$ -CC, ν_e -CC, $\bar{\nu}_e$ -CC and NC categories, while only the former four CC categories are used for the oscillation analysis. ML models categorize the event into the class with the largest probability score value by default. However, as mentioned previously, this default classification may not be optimal for oscillation analysis. Different thresholds on the probability scores can be applied, causing events to migrate among the categories, leading to different signal efficiency and background contamination in each category. Since these event categories are sensitive to oscillation parameters in different ways, this will finally lead to different oscillation sensitivities. For future atmospheric neutrino oscillation analysis, the optimal thresholds on the scores should be tuned to achieve the best sensitivity. It is for the same reason that the ROC curve and AUC values are chosen to represent the identification performances in this work instead of more conventional benchmarks such as signal efficiency and purity.

C. Alternative classification strategy

As described in Sec. III, the baseline strategy of this work is to do the μ -like vs e -like vs NC-like 3-label classification first, followed by the $\nu/\bar{\nu}$ 2-label classification for the identified μ -like and e -like events. Thus, this strategy is referred to as the 3+2-label strategy. Alternatively, the task can also be achieved by doing the ν_e -CC/ $\bar{\nu}_e$ -CC/ ν_μ -CC/ $\bar{\nu}_\mu$ -CC/NC classification all at once using both the PMT features from the prompt trigger and the delayed trigger information, referred to as the 5-label strategy. To test this 5-label strategy, the models used for the 2-label classifications are retrained with the same primary trigger and neutron-capture information inputs, and the model architectures remain the same except the outputs are changed to five scores representing the probability of the event being $\nu_\mu/\bar{\nu}_\mu/\nu_e/\bar{\nu}_e$ /NC-like. The performance is then tested using the same Honda-flux sample and compared with the 3+2-label results using the total AUC scores described in section IV for the two different neutron-capture information handling strategies individually. To have a fair comparison, both the PMT features from the primary trigger and the neutron-capture information are also used for the 3-label classification in the 3+2-label strategy. The total average AUC comparisons of the two strategies are shown in Fig. 15, and consistent performances are observed.

VI. SUMMARY

A machine-learning-based method for the flavor identification and $\nu/\bar{\nu}$ discrimination of atmospheric neutrinos

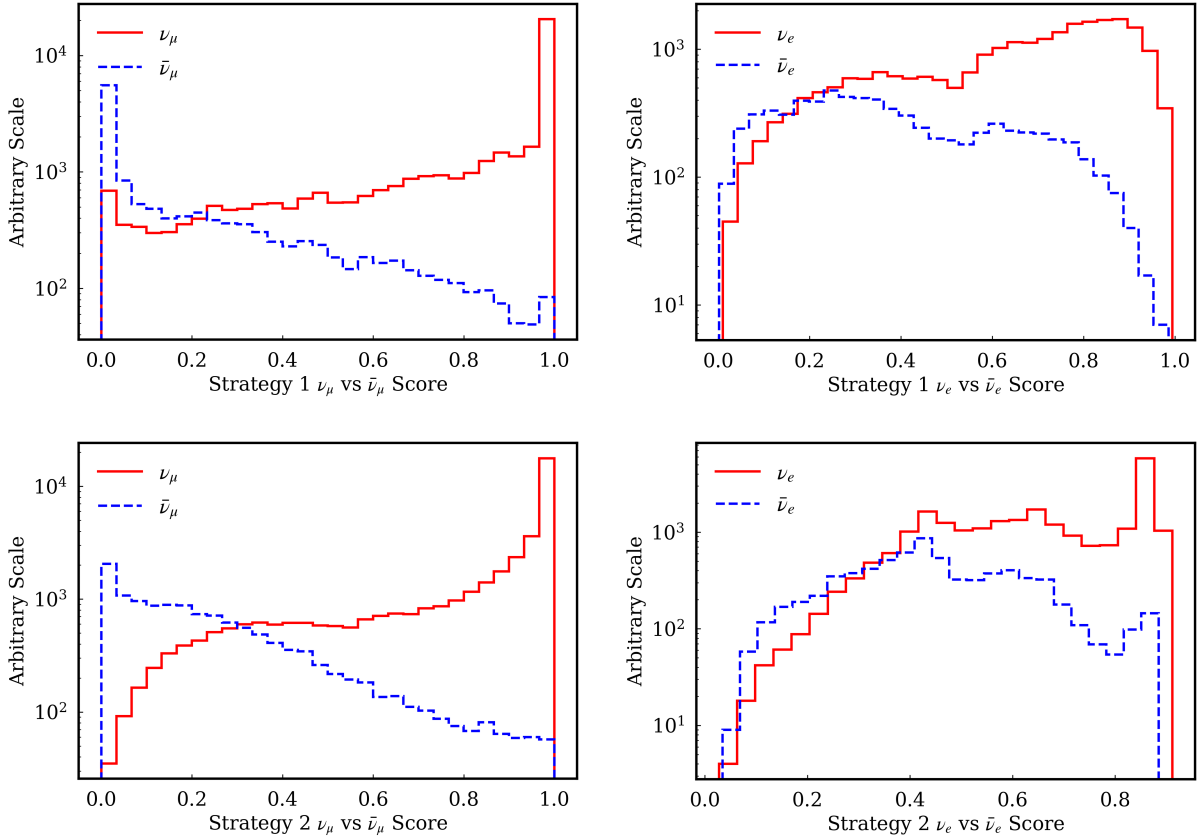


Figure 11. The distributions of ν_μ vs $\bar{\nu}_\mu$ (left) score and ν_e vs $\bar{\nu}_e$ (right) score by strategy 1 (top) and 2 (bottom).

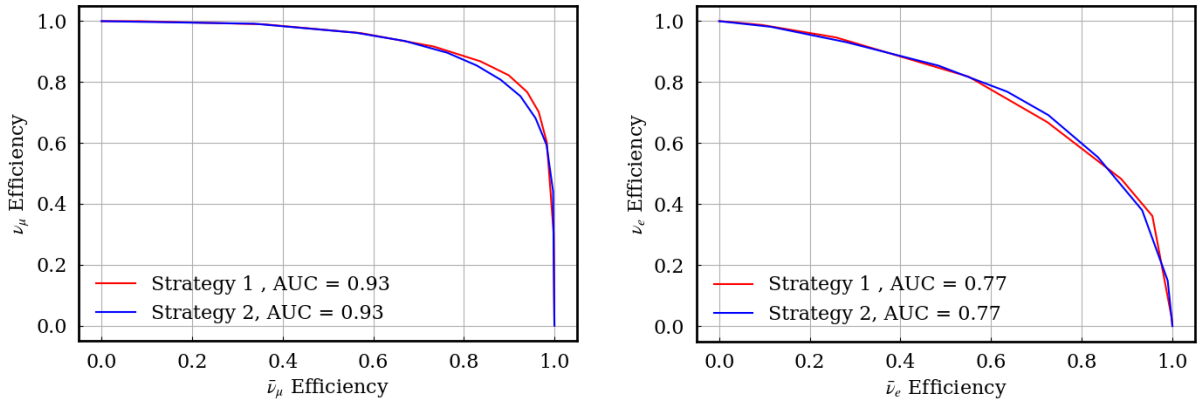


Figure 12. ROC curves of the ν_μ vs $\bar{\nu}_\mu$ (left) and ν_e vs $\bar{\nu}_e$ (right) identification. The vertical axis represents the selection efficiency of neutrinos by varying cut values on the score shown in Fig. 11, and the horizontal axis represents the efficiency of the antineutrinos. The corresponding AUC values are also listed.

in a large homogeneous LS detector is presented in this paper. It utilizes both the features extracted from PMT waveforms in the prompt trigger and the neutron-capture information in the decayed triggers, taking advantage of LS detectors' low threshold measurements of both the charged lepton and hadrons in a neutrino-nucleus inter-

action and the capability of high-efficiency neutron tagging. PMT features from the prompt trigger can capture different topologies of e -like/ μ -like/NC-like events, leading to excellent neutrino flavor identification. Moreover, they also contain the y_{vis} information, which, combined with the neutron-capture information from the delayed

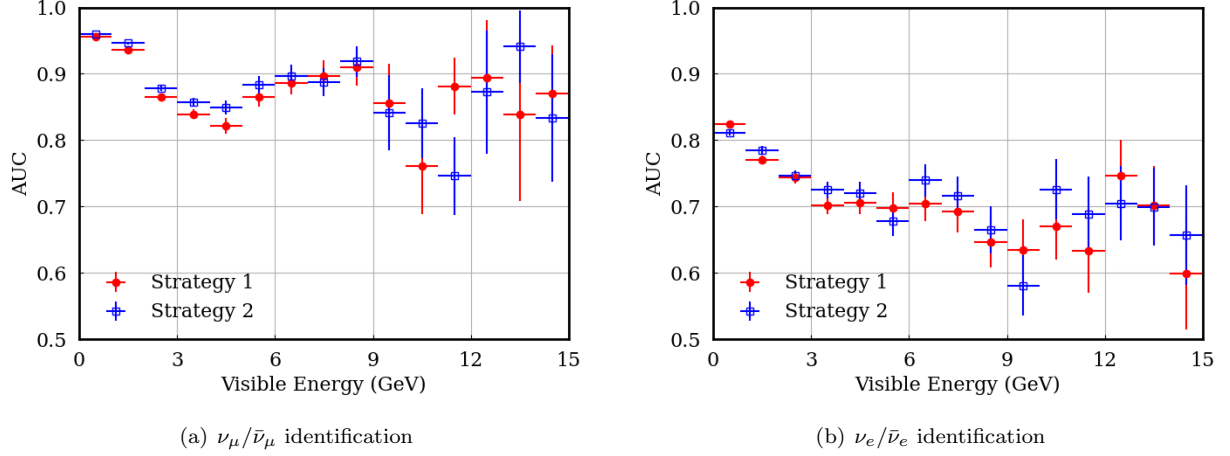


Figure 13. Comparison of the AUC values for the 2-label (a) $\nu_\mu/\bar{\nu}_\mu$ and (b) $\nu_e/\bar{\nu}_e$ identifications as functions of visible energy between the two strategies.

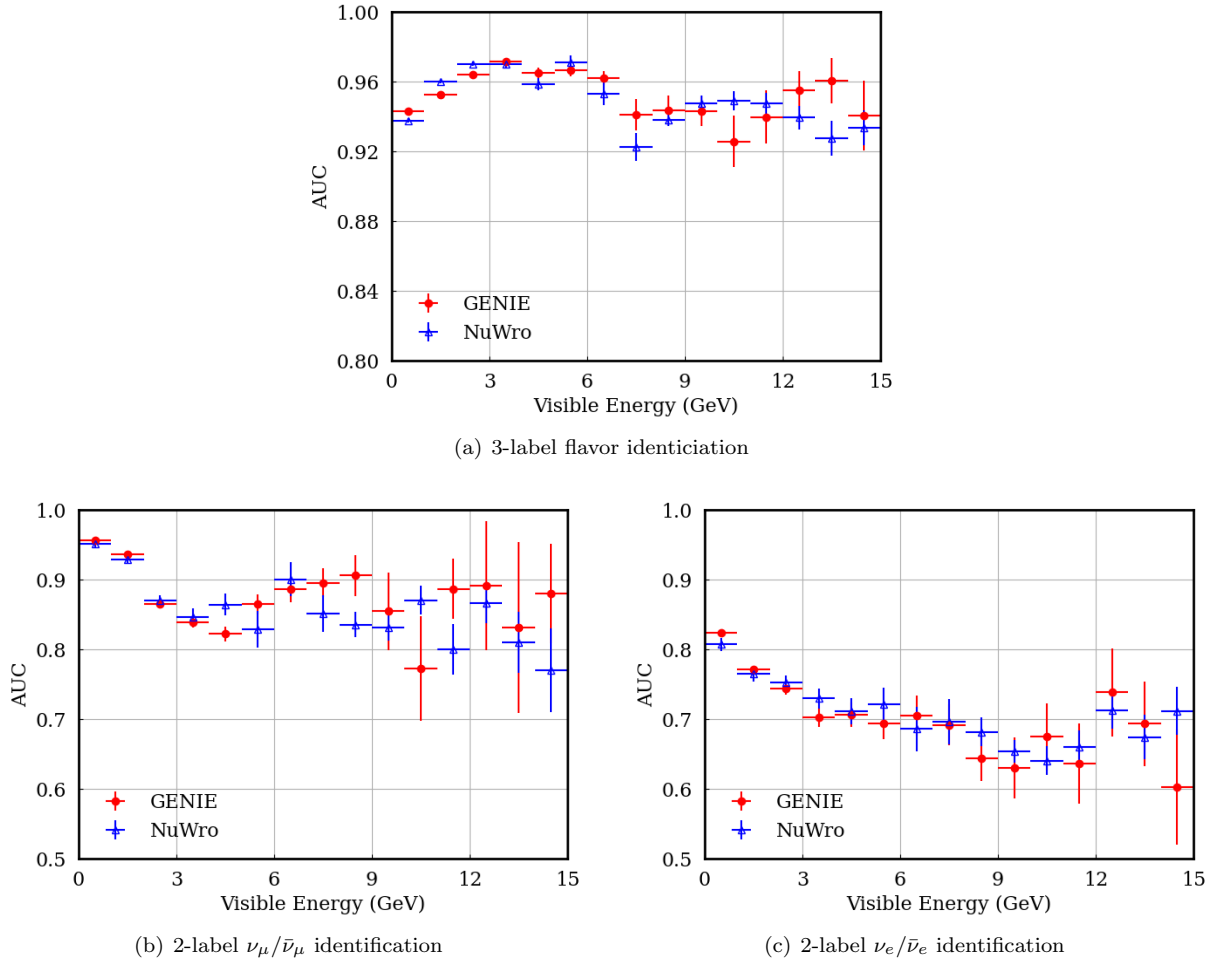


Figure 14. Comparison of the PID performance using the GENIE-generated Honda-flux sample and the NuWro sample. Both (a) 3-label flavor identification and 2-label (b) $\nu_\mu/\bar{\nu}_\mu$, (c) $\nu_e/\bar{\nu}_e$ identifications are shown. The PointNet++ model and strategy 1 of neutron-capture information handling are used.

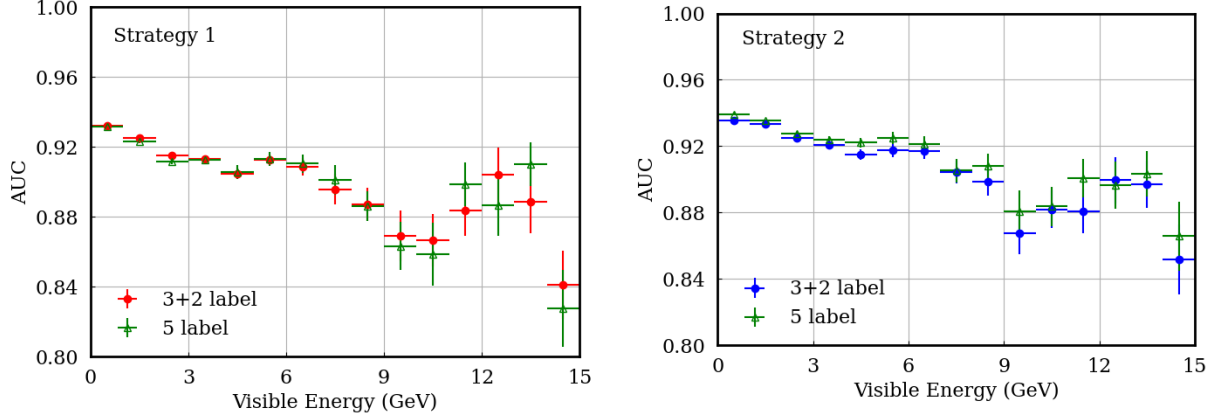


Figure 15. Comparison of the PID performance between 5-label and 3+2 label strategies for the two different neutron information handling strategies.

triggers, exhibit good separation power between ν and $\bar{\nu}$. Different ML models, neutron-capture information handling strategies, and event generators are tested and show consistent performances. Using JUNO as an example, we demonstrate for the first time that large homogeneous LS detectors can perform identification of the atmospheric neutrino flavor and neutrino/antineutrino discrimination with their unique advantages. Combined with excellent energy resolution and directional measurement capability for neutrinos reported in [28], LS detectors such as JUNO can provide competitive results for future atmospheric neutrino oscillation measurements.

ACKNOWLEDGEMENTS

This work was partially supported by CAS Project for Young Scientists in Basic Research (Grant No.YSBR-

099), by the National Natural Science Foundation of China (Grant No.12275160, No.12105158, No.12025502, No.12405230), by National Key R&D Program of China (Grant No.2024YFE0110500), and by Shandong Provincial Natural Science Foundation (Grant No.ZR2022MA062, No.ZR2024QA127). We would also like to thank the Computing Center of the Institute of High Energy Physics, Chinese Academy of Science, and the Key Laboratory of Particle Physics and Particle Irradiation of Ministry of Education, Shandong University for providing the GPU resources.

-
- [1] Y. Fukuda *et al.* (Super-Kamiokande Collaboration), *Phys. Rev. Lett.* **81**, 1562 (1998).
[2] L. Wolfenstein, *Phys. Rev. D* **17**, 2369 (1978).
[3] S. P. Mikheev and A. Y. Smirnov, *Nuovo Cim. C* **9**, 17 (1986).
[4] K. Abe *et al.*, (2011), [arXiv:1109.3262 \[hep-ex\]](https://arxiv.org/abs/1109.3262).
[5] K. Abe *et al.* (Hyper-Kamiokande Collaboration), (2018), [arXiv:1805.04163 \[physics.ins-det\]](https://arxiv.org/abs/1805.04163).
[6] S. Adrian-Martinez *et al.* (KM3Net Collaboration), *J. Phys. G* **43**, 084001 (2016).
[7] S. Aiello *et al.* (KM3NeT), *Eur. Phys. J. C* **82**, 26 (2022).
[8] A. Ishihara (IceCube), *PoS ICRC2019*, 1031 (2021).
[9] F. An *et al.* (JUNO Collaboration), *J. Phys. G* **43**, 030401 (2016).
[10] A. Abusleme *et al.* (JUNO Collaboration), *Progress in Particle and Nuclear Physics* **123**, 103927 (2022).
[11] M. G. Aartsen *et al.* (IceCube-Gen2 Collaboration), *Phys. Rev. D* **101**, 032006 (2020).
[12] A. Cabrera *et al.*, *Sci. Rep.* **12**, 5393 (2022), [arXiv:2008.11280 \[hep-ph\]](https://arxiv.org/abs/2008.11280).
[13] S. Aiello *et al.* (KM3NeT and JUNO Collaborations), *JHEP* **03**, 055.
[14] K. Eguchi *et al.* (KamLAND Collaboration), *Phys. Rev. Lett.* **90**, 021802 (2003).
[15] C. Arpesella *et al.* (Borexino Collaboration), *Phys. Rev. Lett.* **101**, 091302 (2008).
[16] M. Agostini *et al.* (Borexino Collaboration), *Nature* **562**, 505 (2018).
[17] F. P. An *et al.* (Daya Bay Collaboration), *Phys. Rev. Lett.* **108**, 171803 (2012).
[18] F. P. An *et al.* (Daya Bay Collaboration), *Phys. Rev. Lett.* **130**, 161802 (2023), [arXiv:2211.14988 \[hep-ex\]](https://arxiv.org/abs/2211.14988).
[19] J. K. Ahn *et al.* (RENO Collaboration), *Phys. Rev. Lett.* **108**, 191802 (2012), [arXiv:1204.0626 \[hep-ex\]](https://arxiv.org/abs/1204.0626).
[20] G. Bak *et al.* (RENO Collaboration), *Phys. Rev. Lett.* **121**, 201801 (2018), [arXiv:1806.00248 \[hep-ex\]](https://arxiv.org/abs/1806.00248).

- [21] Y. Abe *et al.* (Double Chooz Collaboration), *Phys. Rev. Lett.* **108**, 131801 (2012), arXiv:1112.6353 [hep-ex].
- [22] H. de Kerret *et al.* (Double Chooz Collaboration), *Nature Phys.* **16**, 558 (2020), arXiv:1901.09445 [hep-ex].
- [23] T. Wester *et al.* (Super-Kamiokande Collaboration), *Phys. Rev. D* **109**, 072014 (2024).
- [24] K. Abe *et al.* (Super-Kamiokande Collaboration), *Nucl. Instrum. Meth. A* **1027**, 166248 (2022), arXiv:2109.00360 [physics.ins-det].
- [25] K. Abe *et al.* (Super-Kamiokande Collaboration), *Nucl. Instrum. Meth. A* **1065**, 169480 (2024).
- [26] M. Ribordy and A. Y. Smirnov, *Phys. Rev. D* **87**, 113007 (2013).
- [27] S. G. Olavarrieta, M. Jin, C. A. Argüelles, P. Fernández, and I. Martínez-Soler, *Phys. Rev. D* **110**, L051101 (2024).
- [28] Z. Yang *et al.*, *Phys. Rev. D* **109**, 052005 (2024).
- [29] A. Abusleme *et al.* (JUNO Collaboration), *Eur. Phys. J. Plus* **139**, 1128 (2024).
- [30] T. Lin *et al.*, *Eur. Phys. J. C* **83**, 382 (2023), [Erratum: *Eur.Phys.J.C* 83, 660 (2023)].
- [31] A. Coppi *et al.*, *Nucl. Instrum. Meth. A* **1052**, 168255 (2023).
- [32] C. Cao *et al.*, *Nucl. Instrum. Meth. A* **1005**, 165347 (2021).
- [33] A. Abusleme *et al.* (JUNO Collaboration), *Nucl. Instrum. Meth. A* **988**, 164823 (2021).
- [34] C. Andreopoulos, C. Barry, S. Dytman, H. Gallagher, T. Golan, R. Hatcher, G. Perdue, and J. Yarba, (2015), arXiv:1510.05494 [hep-ph].
- [35] Tena-Vidal *et al.* (GENIE Collaboration), *Phys. Rev. D* **104**, 072009 (2021).
- [36] T. Golan, J. T. Sobczyk, and J. Zmuda, *Nucl. Phys. B Proc. Suppl.* **229-232**, 499 (2012).
- [37] S. Agostinelli *et al.* (GEANT4 Collaboration), *Nucl. Instrum. Meth. A* **506**, 250 (2003).
- [38] J. Allison *et al.*, *IEEE Trans. Nucl. Sci.* **53**, 270 (2006).
- [39] M. Honda, M. S. Athar, T. Kajita, K. Kasahara, and S. Midorikawa, *Phys. Rev. D* **92**, 023004 (2015).
- [40] N. Wiener, *Extrapolation, Interpolation, and Smoothing of Stationary Time Series* (The MIT Press, 1964).
- [41] Y. Huang, J. Chang, Y. Cheng, Z. Chen, J. Hu, X. Ji, F. Li, J. Li, Q. Li, X. Qian, S. Jetter, W. Wang, Z. Wang, Y. Xu, and Z. Yu, *Nuclear Instruments and Methods in Physics Research Section A: Accelerators, Spectrometers, Detectors and Associated Equipment* **895**, 48 (2018).
- [42] N. Perraudin, M. Defferrard, T. Kacprzak, and R. Sgier, *Astronomy and Computing* **27**, 130 (2019).
- [43] C. R. Qi, L. Yi, H. Su, and L. J. Guibas, in *Advances in Neural Information Processing Systems*, Vol. 30 (Curran Associates, Inc., 2017).
- [44] G.-h. Huang, W. Jiang, L.-j. Wen, Y.-f. Wang, and W.-M. Luo, *Nucl. Sci. Tech.* **34**, 83 (2023).
- [45] Y. Wang, Y. Sun, Z. Liu, S. E. Sarma, M. M. Bronstein, and J. M. Solomon, *ACM Transactions on Graphics (tog)* **38**, 1 (2019).
- [46] J. Hanley and B. McNeil, *Radiology* **143**, 29 (1982).
- [47] B. Efron, *The Annals of Statistics* **7**, 1 (1979).